

Article

# Historical aerial surveys map long-term changes of forest cover and structure in the central Congo Basin

Koen Hufkens<sup>1,2,\*</sup> , Thalès de Haulleville<sup>3</sup>, Elizabeth Kearsley<sup>1</sup>, Kim Jacobsen<sup>2,3</sup>, Hans Beeckman<sup>3</sup>, Piet Stoffelen<sup>4</sup>, Filip Vandelook<sup>4</sup>, Sofie Meeus<sup>4</sup>, Michael Amara<sup>5</sup>, Leen Van Hirtum<sup>5</sup>, Jan Van den Bulcke<sup>1</sup>, Hans Verbeeck<sup>1</sup>, Lisa Wingate<sup>2</sup>

<sup>1</sup> Ghent University, Ghent, Belgium;

<sup>2</sup> INRA, UMR ISPA, Villeneuve d'Ornon, France;

<sup>3</sup> Royal Museum for Central Africa, Tervuren, Belgium;

<sup>4</sup> Botanic Garden Meise, Meise, Belgium;

<sup>5</sup> National Archives of Belgium, Brussels, Belgium;

\* Correspondence: koen.hufkens@gmail.com

Academic Editor: name

Version December 30, 2019 submitted to Remote Sens.

**1 Abstract:** Land Use and Land Cover change (LULCC) of African rainforest contribute to global carbon  
2 emissions. Yet, most historical estimates of LULCC and their carbon emissions rely on non-spatially  
3 explicity data in the pre-satellite era (< 1972). Past studies have expanded this pre-satellite time  
4 frame with declassified satellite surveillance data or aerial surveys, but none cover the Congo Basin.  
5 Here, we use historical aerial survey photos to map the extent and structure of LULCC around  
6 Yangambi, central Congo Basin, in 1958. Our study leveraged Structure-from-Motion to generate  
7 a large orthomosaic covering 828 km<sup>2</sup>, counting 733 million pixels, at a sub meter resolution and  
8 geo-referenced to ~4.7 ± 4.3 m. Primary forest in the orthomosaic was classified with a Convolutional  
9 Neural Network Deep Learning approach. We used these data to quantify LULCC, landscape  
10 and canopy complexity and scale above ground biomass between historical and contemporary  
11 condition. We show a shift from historical highly structured industrial deforestation in 1958 (162  
12 km<sup>2</sup>), to contemporary smallholder farming clearing (88 km<sup>2</sup>), increasing landscape fragmentation  
13 and forest edges. Efforts to quantify canopy texture and their link to carbon storage had limited to  
14 no success. Our analysis provides an insight in key spatial and temporal patterns of deforestation  
15 and reforestation at a multi-decadal scale and provide a historical context to land-cover and land-use  
16 change spatial patterns for past and ongoing field research in the area.

**17 Keywords:** Aerial survey, data recovery, CNN, Deep Learning, SfM, Congo Basin

## 18 1. Introduction

19 The functioning of a tropical forest, and its capacity to sequester carbon, is heavily influenced  
20 by anthropogenic disturbances such as selective logging, clear felling, or slash and burn practices, all  
21 increasing forest fragmentation. This increased pace in the loss of rainforest cover [1] is predicted to  
22 negatively impact the function of these tropical forests, and their future capacity to sequester carbon,  
23 as anthropogenic disturbances such as selective logging, clear felling, or slash and burn practices  
24 collectively contribute to increasing forest fragmentation.

25 These forest fragments and their edges contain fewer large trees [2], in part due to their hotter and  
26 brighter microclimates [3]. Similarly, species composition and biodiversity [4] are negatively affected.  
27 Spatial disturbances also have an explicit temporal component, where the time since disturbance  
28 affects the strength of the effects [5]. Deforestation and gap formation also influence the overall canopy  
29 structure, where pioneer species grow taller and with narrower crowns [4,6] affecting the forest light  
30 regime and carbon dynamics [7]. As such, anthropogenic factors through land-use and land cover  
31 change (LULCC) heavily affect forest structure and functioning [5,8,9]. In the tropics the majority of  
32 emissions originate from deforestation and forest degradation [10–12] contributing to 10–15% of the  
33 total global emissions [13] and concomitant losses in biodiversity losses [14,15] and how LULCC is  
34 evolving over time. Although the African rainforest is the second largest on Earth and covers ~630  
35 million ha, representing up to 66 Pg of carbon storage [16], and currently loses forest at an increasing  
36 pace [1]. Yet, the tropics is now becoming a large source of CO<sub>2</sub> to the atmosphere as deforestation and  
37 forest degradation [10–12] contribute up to 10–15% of the total global CO<sub>2</sub> emissions [13]. Furthermore,  
38 recent estimates show that 31% of recent carbon emissions are caused by edge effects alone [9]. In  
39 this context, there are very few long term forest inventory plots that presently exist in the central  
40 Congo Basin [17,18]. This further limits the accuracy of current biomass estimates and challenges  
41 our understanding of how forest structure and function changes in the short and long term in these  
42 ecosystems [19,20].

43 Historical estimates of LULCC, and their carbon emissions, exist [11,21–23], however they  
44 generally rely on non-spatially explicit data in the pre-satellite era (< 1972) [24]. These analysis  
45 often use FAO statistics, historical land-use sources, and/or population and socio-economic data [11],  
46 as limited earlier spatial data sources are available [10,25]. For example, the Houghton [24] long-term  
47 study used FAO and national censuses alongside a bookkeeping model to estimate carbon emissions  
48 from LULCC. Other studies use remote sensing data, but are limited in time to recent decades [11,22].  
49 These proxy based studies have a limited view on long-term direct and indirect spatial effects of  
50 deforestation. As such, both the spatial structure and the fragmentation pattern of a forest combined

51 with its life history has a profound effect on carbon emssions. However, in this context remote  
52 sensing assessments provide more accurate spatial information to help estimate carbon emissions [26].

53 Past studies expanded knowledge during the pre-satellite time frame through the use of now  
54 declassified satellite surveillance data to map deforestation in the US, central Brazil, and post world war  
55 II Germany [27,28]. In some cases these records could extend back in time even further using historical  
56 aerial survey images. In northern Europe especially these data are well known and used, for example  
57 to map the extent of forest cover across ~100 km<sup>2</sup> regularly, and at times using automated workflows  
58 [29]. Survey data across the African continent is less common or inaccessible or both. Some studies  
59 do exist, both Buitenwerf *et al.* [30] and Okeke and Karniel [31] used aerial survey images to map  
60 vegetation changes in South African savannas and the Adulam Nature Reserve, respectively. Whilst  
61 Frankl *et al.* [32] used 20 aerial survey images to map the Ethiopian highlands of 1935. High resolution  
62 aerial or surveillance satellite images provide scientists tools to monitor forest extent and structure over  
63 long time frames. Moreover, canopy texture from aerial survey images has been successfully linked  
64 to above ground biomass [33–35]. Thus using texture based metrics obtained from (high resolution)  
65 remote sensing data opens up possibilities to link historical aerial footage to carbon density across  
66 large spatial extents [34].

67 Given the impact of LULCC on the structure and functioning of tropical forests, and their influence  
68 on both carbon dynamics [19] and biodiversity [15], accurate long term reporting of historical forest  
69 cover in the pre-satellite era is an imperative [36]. In this study we use a combination of historical  
70 aerial photography and contemporary remote sensing data to map long-term changes in the extent  
71 and structure of the tropical forest surrounding Yangambi, in the central Congo Basin at the beginning  
72 of 1958 and the start of the antrophocene [37]. Our analysis provides a historical insight into important  
73 LULCC spatial patterns in Yangambi, such as fragmentation and edge complexity. Our analysis further  
74 contextualises the influence of changes in the forest's life history on past and current research into  
75 Above Ground Carbon (AGC) storage [19] and biodiversity [15] in the central Congo Basin.

## 76 2. Methods

### 77 2.1. Historical data acquisition

78 Data for the central Congo Basin region, surrounding Kisangani, were collected in several flights  
79 during the dry season of 1958 and 1959 (from 8/01/1958 to 20/02/1958 and from 28/12/1958 to  
80 9/01/1959 respectively, see Appendix Figure 1) to generate topographic maps of the area, supervised  
81 by the “Institut Géographique du Congo Belge” in Kinshasa (then Léopoldville). Black-and-White  
82 infrared images (0.4 - 0.9 μm) were gathered along flight paths running mostly from west to east,  
83 between 9 - 11h local time. Along a flight path continuous images were taken using a Wild Heerburgg

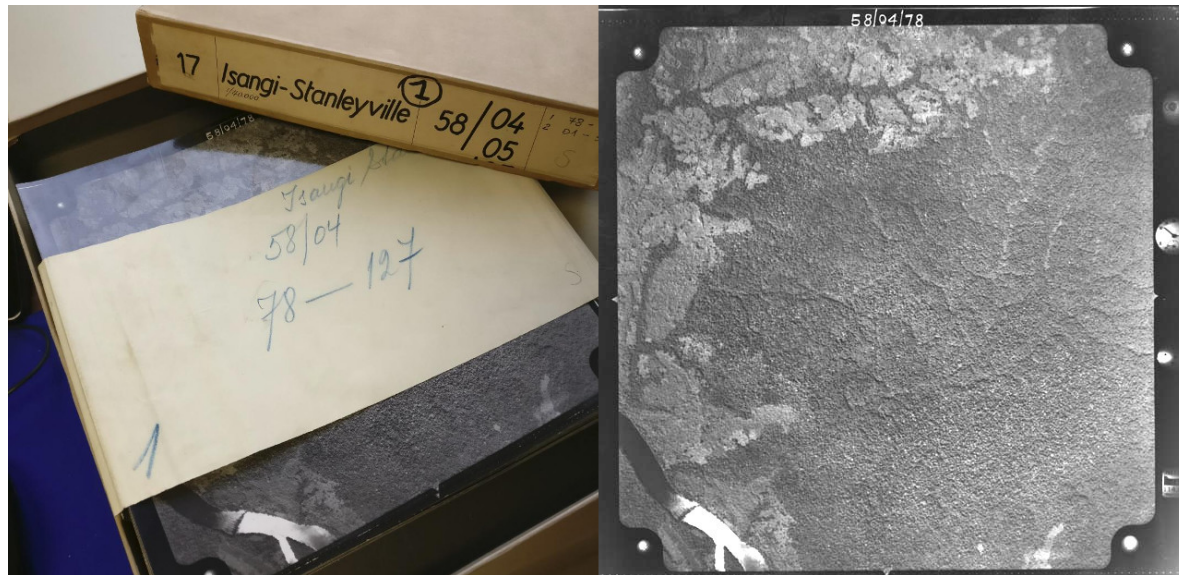


**Figure 1.** A box of historical aerial photographs (left) and a single aerial photograph (right) showing part of the Congo river. Note the meta-data provided in the margins of the image such as acquisition time and flight height and the solar glare on the Congo river.

84 RC5a (currently Leica Geosystems) with an Aviogon lens assembly (114.83mm / f 5.6, with a 90° view  
 85 angle) resulting in square photo negative of 180 by 180 mm. Flights were flown at an average absolute  
 86 altitude of ~5200 m above sea level, covering roughly 18 530 km<sup>2</sup> at an approximate scale of 1/40  
 87 000. The use of the integrated autograph system ensured timely acquisition of pictures with a precise  
 88 overlap (~1/3) between images. This large overlap between images together with flight parameters  
 89 would allow post-processing, using stereographs, to create accurate topographic maps. Original data  
 90 from this campaign are stored in the [Royal Museum for Central Africa](#) in Tervuren, Belgium (Figure 1).

## 91 2.2. Site selection

92 We prioritised flight paths and images that contained current day permanent sampling plots,  
 93 larger protected areas, and past agricultural and forest research facilities (Figure 2). This selection  
 94 provides a comprehensive mapping of the Yangambi area and the life history of the forest surrounding  
 95 it. Thereafter, we selected flight paths 1 through 11 for digitization. From this larger dataset of 334  
 96 images we selected 74 survey images for orthomosaic compositing and further analysis. All the  
 97 selected images stem from the flight campaign made during January and February of 1958. The area  
 98 includes the Yangambi village, 20 contemporary permanent sampling plots [19], past and present  
 99 agricultural experimental plots [38] and large sections of the Yangambi **UNESCO Man and Biosphere**  
 100 **reserve** surrounding to the west and east of the village. Although not formally mosaicked we provided  
 101 a full dataset of pre-processed images using the cropping and normalization routines described below.  
 102 The latter data was not used in subsequent LULCC analysis, but has been archived and made available  
 103 to the public separately (see code & data availability statement below).

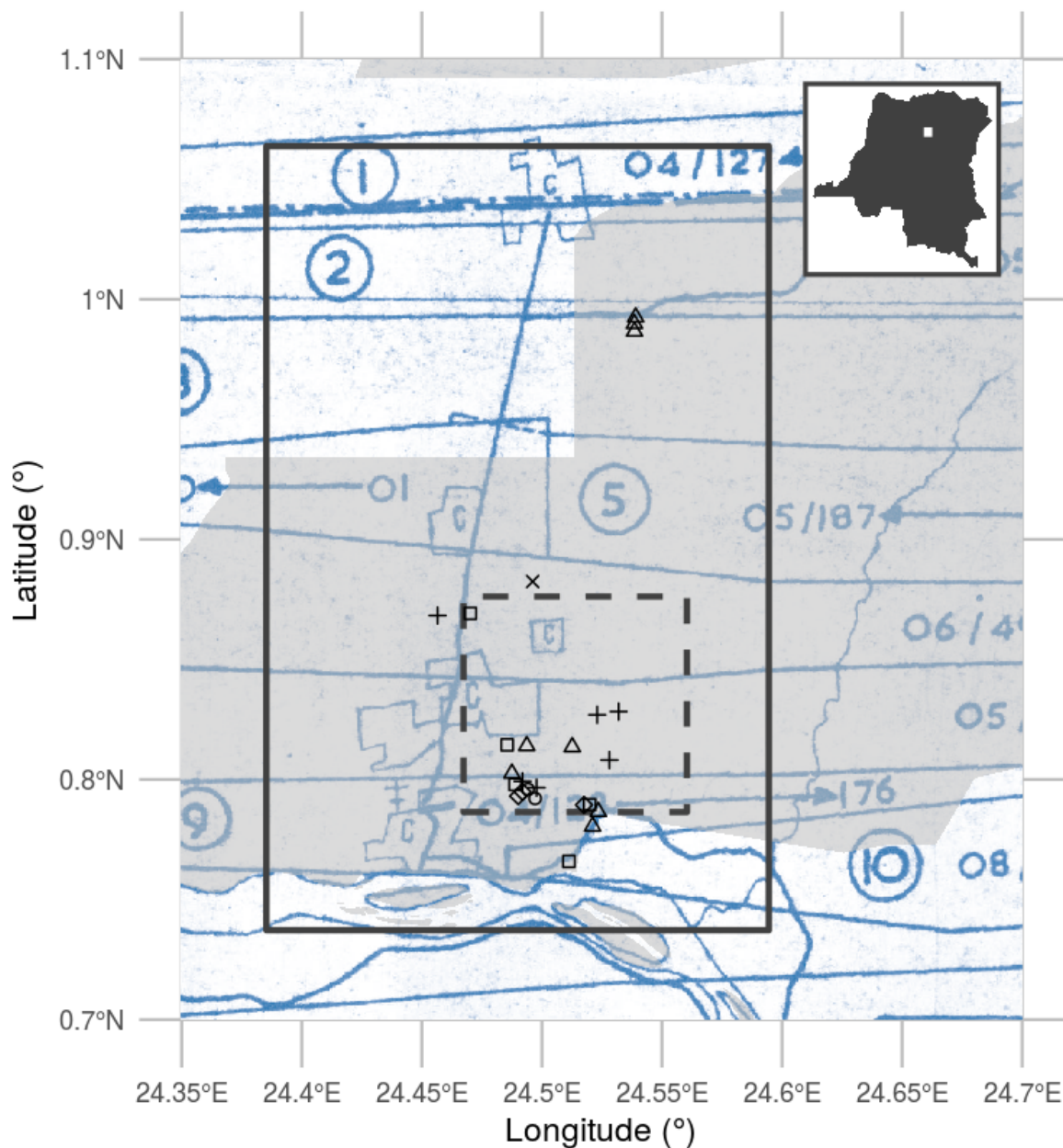


**Figure 2.** Overview of the historical flight paths during aerial photo acquisition and ancillary data used in this study. The bounding box of the orthomosaic data presented in this study is shown as a rectangle (23x36 km). The outline of a recent high-resolution Geo-eye panchromatic image is shown as a dashed dark grey rectangle (10x10km). The location of various permanent sampling plots are shown as x, +, and open squares and triangles for the mixed, mono-dominant and edge plots respectively. The grey polygon delineates the current day Yangambi Man and Biosphere reserve. The inset, top right, situates the greater Yangambi region with the DR Congo. The full flight plan and details are shown in Appendix Figure 1 and 2

104    2.3. *Digitization and data processing*

105    All selected images, covering the Yangambi area, were contact prints as original negatives of the  
106    prints were not available. Images were scanned at a resolution exceeding their original resolution  
107    (or grain) at the maximal physical resolution of an Epson A3 flatbed scanner (i.e. 2400 dpi or 160MP  
108    per image) and saved as lossless tiff images. Data were normalized using contrast limited histogram  
109    equalization [39] with a window size of 32 and a clip limit of 1.5. Fiduciary marks were used to rectify  
110    and downsample the images into square 7700x7700 pixel images (~1200 dpi, 81MP). This resulted in a  
111    dataset with digital images at a resolution that remained above the visible grain of the photographs,  
112    whilst the reduced image size facilitated easier file handling and processing speed.

113    Data was processed into a georeferenced orthomosaic using a Structure from motion (SfM, Ullman  
114    [40]) approach implemented in [Agisoft Metashape](#) version 1.5.2 (Agisoft LLC, St. Petersburg, Russia).  
115    An orthomosaic corrects remote sensing data to represent a perfectly downward looking image, free  
116    from perspective distortions due to topography and camera tilt. Using the SfM technique features,  
117    areas in images with a large degree of similarity, are matched across various images to reconstruct  
118    a three dimensional scene (topography) from two-dimensional image sequences. During the SfM  
119    analysis we masked clouds, glare or large water bodies such as the Congo river.

120    We calculated the orthomosaic using a low resolution point cloud and digital elevation map  
121    (DEM). Additional ground control points were provided to assist in the referencing of image and  
122    constrain the optimization routine used in the SfM algorithm. Ground control points consisted of  
123    rooftop edges of permanent structures which could be verified in both old and new aerial imagery  
124    (i.e. ESRI World Imagery). Although clouds were removed during the SfM routine we did not mask all  
125    clouds in the final orthomosaic to maximize forest coverage. The final scene was cropped, to provide  
126    consistent wall to wall coverage of the reconstructed scene. The orthomosaic was exported as a geotiff  
127    for further georeferencing in QGIS [41] using the georeferencer plugin (version 3.1.9) and additional  
128    ESRI World Imagery high resolution reference data. We used 3<sup>rd</sup> degree polynomial and 16 ground  
129    control points to correct the final image. Ground control points, raw image data and final processed  
130    image are provided in addition to measures of uncertainty such as mean root mean squared (RMSE),  
131    mean and median error across all ground control points. All subsequent analysis are executed on the  
132    final geo-referenced orthomosaic or subsets of it.

133 2.4. Land-Use and Land-Cover Change

134 2.4.1. Classifying forest cover

135 We automatically delineated all natural forest in the historical data, thus excluding tree plantations,  
136 thinned or deteriorated forest stands, fields and buildings. We used the Unet Convolutional Neural  
137 Net (CNN, Ronneberger *et al.* [42]) architecture implemented in Keras [43] with an efficientnetb3  
138 pre-processing backbone [44] running on TensorFlow [45] to train a binary classifier (i.e. forest or  
139 non-forested). This methodology is increasingly being used to automate pixel-level classification in  
140 (color) digital photography data [46]. Training data were collected from the orthomosaic by randomly  
141 selecting 513 pixel square tiles from homogeneous forested or non-forested areas within the historical  
142 orthomosaic. Homogeneous tiles were combined in synthetic landscapes using a random gaussian  
143 field based binary mask (Figure 3). We generated 5000 synthetic landscapes for training, while 500  
144 landscapes were generated for both the validation and the testing dataset. Source tiles did not repeat  
145 across datasets to limit overfitting. In order to limit stitch line misclassifications, along the seams of  
146 mosaicked images, we created synthetic landscapes with different forest tiles to mimick forest texture  
147 transitions. We applied this technique to 10% of the generated synthetic landscapes. The CNN model  
148 was trained for 100 epochs with a batch size of 30 using Adam optimization [47], maximizing the  
149 Intersect-over-Union (IoU) using Sørensen–Dice and categorical cross-entropy loss functions. Data  
150 augmentation included random cropping to 320 pixel squares, random orientation, scaling, perspective,  
151 contrast and brightness shifts and image blurring. During final model evaluation we report the IoU of  
152 our out-of-sample test datasets. The optimized model was used to classify the complete orthomosaic  
153 using a moving window approach with a step size of 110 pixels and a majority vote across overlapping  
154 areas to limit segmentation edge effects. We refer to Figure 4 for a synoptic overview of the full  
155 deep learning learning workflow. In addition, we used the first acquisition of a recent pan-chromatic  
156 Geo-Eye 1 stereo pair (GeoEye, 2012, Thornton, Colorado, U.S.A., order 737537, 2011-11-11 8:55h GMT  
157 or 9:55h local time) to classify and visually assess the robustness of the algorithm on contemporary  
158 remote sensing imagery with the same moving window approach.

159 To map long term land-use and land-cover change in the Yangambi region we used the  
160 contemporary Global Forest Change version 1.6 data (GFC, tile 10N-020E) [10]. Using this data  
161 we calculated the latest state of the forest with respect to the conditions at the start of 1958, 60 years  
162 earlier. In our analysis we only included forested pixels which recorded no loss throughout the whole  
163 2000 - 2018 period. As the resolution of the historical forest classification exceeds that of the GFC map  
164 we downsampled our historical forest cover data to 30m GFC resolution. We masked out all water  
165 bodies using the Global Forest Change survey data mask layer, and limited the analysis to the right

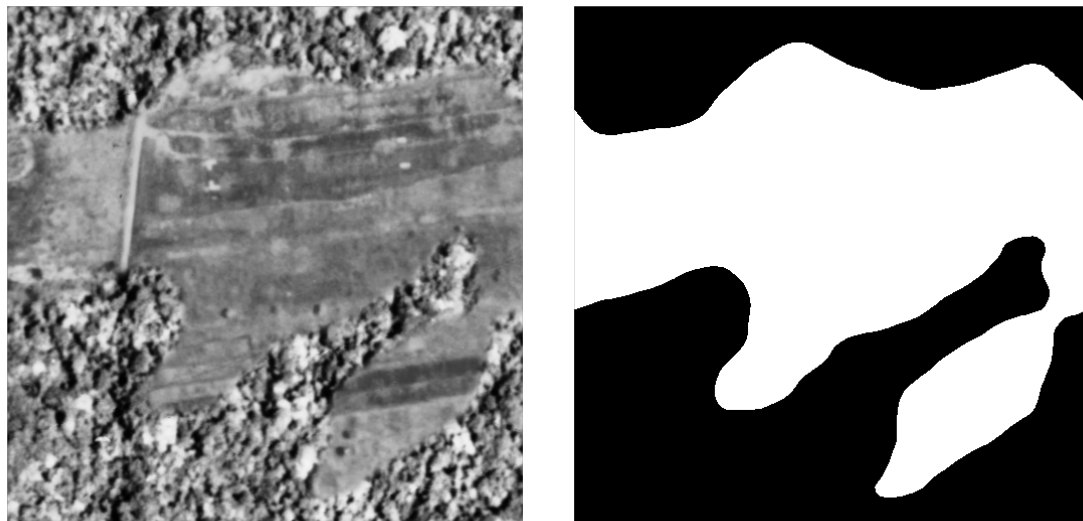


**Figure 3.** An example synthetic landscape, combining homogeneous forest and non-forest images into a patchy landscape using random gaussian field based masks. The left panel shows a combined synthetic landscape, while the right panel shows the corresponding forest (black) and non-forest (white) labels.

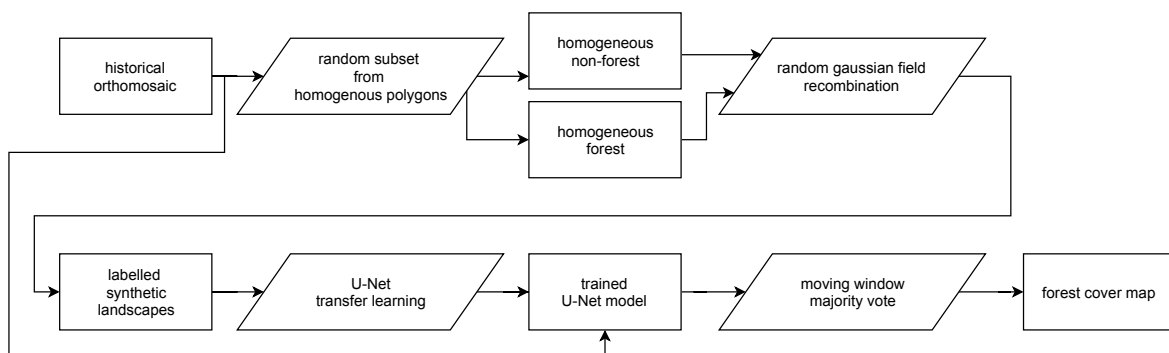


**Figure 4.** A diagram of the deep learning workflow followed in training a binary forest / non-forest cover convolutional neural net U-Net model to generate our forest cover map.

166 bank of the Congo river. Where the datasets overlap we provide summary statistics of deforestation,  
167 reforestation and afforestation. The same methodology was used to quantify CNN model performance  
168 across the Geo-Eye 1 scene.

169 2.4.2. Landscape fragmentation & Above Ground Carbon estimates

170 To quantify changes in the structure of forest cover and its disturbances we used spatial pattern  
171 analysis landscape fragmentation metrics [48]. We report the ratio of edge to area and the fractal  
172 index to quantify landscape complexity of forest disturbances. Statistics were calculated for all forest  
173 disturbance patches larger than 1 ha and smaller than the 95<sup>th</sup> percentile of the patch size distribution  
174 using the R package landscapemetrics [49]. We provide mean and standard deviation on edge, area,  
175 their ratio and fractal dimension for both the historical and contemporary Hansen *et al.* [10] forest  
176 cover maps.

177 We estimated above ground carbon (AGC) losses and gains over time using plot based averages  
178 of recent inventory data at permanent sampling plots in the area (Figure 2). We refer to Kearsley *et al.*  
179 [19] for the survey method and allometric relations used to scale the survey data. Unlike standard  
180 square 1 ha plots edge plots were set back 200m from forest edges and were 50x200m, with the 50m  
181 side of the plot along the forest edge and continuing 200m into the forest (Appendix Table 1). We  
182 further confirmed that forest edge plots did not show a significantly different AGC compared to those  
183 of non-edged / mixed forest plots (Mann Whitney U test,  $p < 0.05$ ). Thus it was not necessary to  
184 explicitly quantify changes in AGC caused by edge effects. Moreover, we used the mean values of the  
185 mixed forest as representative for potential AGC losses. Despite the challenges inherent in quantifying  
186 AGC for forest edges we mapped the total extent of the edges in the contemporary landscape. To  
187 align our landscape analysis with exploratory analysis of the survey data we used a buffer of 200m to  
188 estimate the extent of forest edges and patches, up to the location of forest edge plots.

189 Surveys of old plantations show a large variation in AGC, depending on age and the crop type.  
190 For example, the AGC values varied from 168.67 to 86.55 g Mg C ha<sup>-1</sup>, for *Hevea brasiliensis* (rubber  
191 tree) and *Elaeis guineensis* (oil palm) plots respectively (Bustillo *et al.* [50], personal communications).  
192 These higher values are in line with the mixed AGC estimates in the area, while the palm plantations  
193 resemble old-regrowth values (81.8 Mg C ha<sup>-1</sup>, see Table A1). We therefore use both the estimates  
194 of old-regrowth and mixed forest to estimate AGC for regrowth. We did not have sufficient data to  
195 account for individual changes in AGC across plantations.

196 2.5. Canopy structure & FOTO texture analysis

197 We compared the structure of the canopy both visually and using Fourier Transform Textural  
198 Ordination (FOTO, Couteron [51]). Fourier Transform Textural Ordination uses a principal component

199 analysis (PCA) on radially averaged 2D Fourier spectra to characterize canopy (image) texture. The  
200 FOTO technique was first described by Couteron [51] to quantify canopy stucture in relation to biomass  
201 and biodiversity, and can be used across multiple scenes using normalization [35].

202 We used an area of 400x400m (16 ha) around contemporary permanent sampling plot locations to  
203 quantify the general state of the canopy in both historical and contemporary pan-chromatic Geo-Eye 1  
204 remote sensing data (GeoEye, 2012, Thornton, Colorado, U.S.A., order 737537, 2011-11-11 8:55h GMT or  
205 9:55h local time). Geo-Eye data were resampled to the resolution of the historical data using a nearest  
206 neighbour interpolation for comparison. For permanent sampling plot locations in both historical  
207 and contemporary data a rectangular buffer of 200m around the centre of all plots was used to create  
208 small image subsets. All image subsets were processed using the R based FOTO implementation  
209 and package [52] using global normalization, ensuring intercomparability of texture metrics across  
210 time and space [35]. We used a FOTO (moving) window size of 187 pixels (or ~150m), as described  
211 in Solórzano *et al.* [53] and Barbier *et al.* [35], to ensure that multiple individual canopies could be  
212 included in the analysis. A buffer with a radius of 50m around the center of all permanent sampling  
213 plots was used to determine the average value of the first principle component (PC), explaining the  
214 majority of the variance in canopy texture. Where both the Geo-Eye data and the orthomosaic image  
215 overlapped we processed the intersecting region to explore a wall-to-wall comparison between past  
216 and current canopy texture metrics.

217 We used the standard FOTO methodology with fixed zones, instead of the moving window  
218 approach. The window size was set to the same size (187 pixels or ~150m) as used in the moving  
219 window analysis above. To account for illumination differences between the two scenes we applied  
220 histogram matching. No global normalization was applied, as the scene was processed as a whole. PC  
221 values from this analysis for all permanent sampling plots in both image scences were extracted using  
222 a buffer with a radius of 50m.

223 For both site based and scene analysis we correlate PC values with permanent sample plot  
224 inventory data such as stem density, above ground biomass and tree species richness. Additional  
225 comparisons are made between contemporary Geo-Eye data and the historical orthomosaic derived PC  
226 values. Due to the few available permanent sampling plots in both scenes we used a non-parametric  
227 paired signed rank (Wilcoxon) test to determine differences between the PC values of the Geo-Eye and  
228 historical orthomosaic image scenes across mono-dominant and mixed forest types. In all analysis,  
229 mono-dominant site 4 was removed from the analysis due to cloud contamination.

**230 3. Results**

231 Our analysis provides a first spatially explicit historical composite of aerial survey images  
232 mapping LULCC within the Congo Basin. The use of high resolution historical images combined with  
233 structure from motion image processing techniques allowed us to mosaic old imagery across a large  
234 extent. The final orthomosaic composition of the Yangambi region resulted in an image scene covering  
235 approximately 733 million pixels across ~828 km<sup>2</sup> (~23x36 km, Figure 2). The overall accuracy of the  
236 structure from motion orthomosaic composition was 0.88 m/pixel using the sparse cloud DEM for  
237 corrections at 45.8 m/pixel. The resulting georeferenced scene had a spatial accuracy of approximately  
238 23m. Further georeferencing outside the SfM workflow reduced the mean error at the ground control  
239 points to  $5.3 \pm 4.9$  px (~ $4.7 \pm 4.3$  m), with a median error of 2.9 px (2.6m). The orthomosaic served  
240 as input for all subsequent LULCC analysis with all derived maps provided with the manuscript  
241 repository (see data & code availability statements below).

**242 3.1. Land-use and Land-Cover Change & Above Ground Carbon**

243 Our CNN deep learning classifier reached an Intersection-over-Union (IoU) accuracy of 97% on the  
244 detection of disturbed forest in out-of-sample test data. A visual comparison on recent pan-chromatic  
245 Geo-Eye 1 data shows good agreement, for a total of 87% of all pixels, between the landsat based  
246 GFC data and downscaled CNN results (Appendix Table 3 and Figure 7). Scaling our classifier to the  
247 whole historical orthomosaic we detected 162 km<sup>2</sup> (or ~20% of the scene) of disturbed forests. A large  
248 fraction of the disturbed area was restored in the period between the two acquisitions. In total, 99 km<sup>2</sup>,  
249 or little over half of the affected forest was restored (Figure 5C-D, dark blue). Recent deforested areas,  
250 as registered through satellite remote sensing, approximate 88 km<sup>2</sup> (Table 1, Figure 5C-D / light green).

251 Recent deforestation follows a distinctly different pattern compared to historical patterns.  
252 Historical deforestation showed a classical fishbone pattern for forest clearing with very sharp  
253 edges, while current patterns are patchy and ad-hoc (figure 5D, dark blue and green colours  
254 respectively). These differences are reflected in the analysis of landscape metrics of forest loss.  
255 Between the historical and contemporary LULCC maps we see an increase in small disturbances,  
256 as indicated by the decreasing area of the mean patch size, down to  $\sim 1.86 \pm 0.75$  ha from  $\sim 5.25 \pm$   
257 5.02 ha historically. Perimeter lengths were longer historically, at  $1451.58 \pm 943.27$  m, compared to  
258 contemporary landscapes  $\sim 921.74 \pm 362.59$  m (Table 2). This shift in perimeter area ratio led to a  
259 similar change in the fractal index, increasing in value to  $1.1 \pm 0.05$  from  $1.09 \pm 0.04$  over time. Values  
260 closer to a fractal index of 2 suggest a more complex (fragmented) landscape.

261 A comparison of forest edge plots with mixed forest plots showed no significant difference in  
262 AGC, or other reported values such as species richness, basal area or stem density (Mann Whitney U

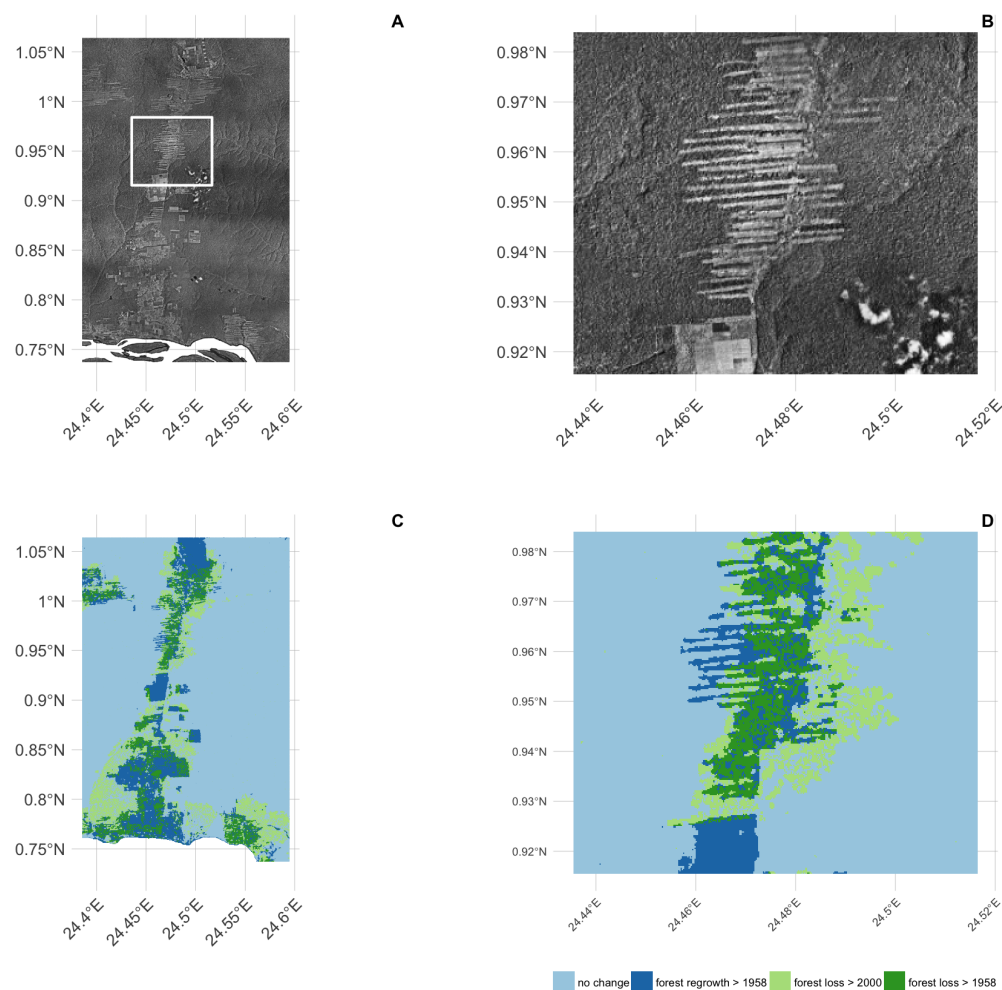


**Figure 5.** Overview of the final orthomosaic of the greater Yangambi region (A), a detailed inset (B) and the derived land use/land cover change map displayed as the difference between a manual classification of the orthomosaic and a recent map by Hansen et al. 2013 (C) and the corresponding land cover map for inset B (D).

<sup>263</sup> test,  $p < 0.05$ ). Edge influence did not extend beyond 200 m from a forest edge, but still represented an  
<sup>264</sup> area of 132 km<sup>2</sup>.

<sup>265</sup> Changes in both land-use and land-cover led to concomitant changes in above ground carbon  
<sup>266</sup> stocks. Recovery throughout the region was characterized for patches of forest and plantations.  
<sup>267</sup> Assuming high density stands, based on previous work, this could amount to a carbon gains of 1592  
<sup>268</sup> Gg C across our study area, offsetting more recent losses of approximately 1408 Gg C. On the other  
<sup>269</sup> hand, at the low end, if we assume a lower carbon density of 81.8 Mg C ha<sup>-1</sup> this would result in a  
<sup>270</sup> total carbon gain of 811 Gg C. Using our approach results indicate that overall deforestation around  
<sup>271</sup> Yangambi has resulted in a loss of ~2416 Gg C in AGC stocks.

**Table 1.** Land use land cover change statistics of forest cover around Yangambi in the central Congo Basin. The data evaluates a difference between a historical (1958) aerial photography based survey and the Hansen et al. 2013 based satellite remote sensing data. Spatial coverage statistics are provided in square kilometers (km) and hectares (ha), rounded to the nearest integer as well as Above Ground Carbon (AGC) scaled using recent survey measurements.

	AGC		
	km <sup>2</sup>	ha	(Gg C ha <sup>-1</sup> )
Forest	685	68455	-
- of which edges	132	13151	-
Regrowth > 1958 loss	99	9918	811 - 1592
Loss > 2000	88	8776	1408
Loss > 1958 (permanent)	63	6282	1008

**Table 2.** Landscape metrics for historical and contemporary deforestation patterns. We report patch perimeter and area, their ratio and fractal dimension. Values are reported as mean  $\pm$  standard deviation, across all deforestation patches.

	perimeter (m)	area (ha)	ratio (m <sup>-1</sup> )	fractal dimension
historical	$1451.58 \pm 943.27$	$5.25 \pm 5.02$	$0.03 \pm 0.01$	$1.09 \pm 0.04$
contemporary	$921.74 \pm 362.59$	$1.86 \pm 0.75$	$0.05 \pm 0.01$	$1.1 \pm 0.05$

### <sup>272</sup> 3.2. Canopy structure & FOTO texture analysis

<sup>273</sup> Visual interpretation of the scenes provide evidence that most locations do not change dramatically  
<sup>274</sup> with respect to canopy composition, except for the large areas of disturbances in contemporary fallow  
<sup>275</sup> or young-regrowth plots. One marked difference is noted in the mono-dominant site 6 (Appendix  
<sup>276</sup> Table 1). Here, the current mono-dominant *Brachystegia laurentii* is a recent development, changing the  
<sup>277</sup> canopy structure visibly during the last half century (Figure 6). The previous varied canopy structure  
<sup>278</sup> gave way to a more dense and uniform canopy. This is reflected in a change of the FOTO PC value from  
<sup>279</sup> 0.19 historically to its current value of 0.54. This historical value is similar to the mean of contemporary  
<sup>280</sup> mono-dominant stands with PC averaging  $0.34 \pm 0.1$ , and is only slightly higher than historical values  
<sup>281</sup> for a mixed forest ( $0.18 \pm 0.08$ ). The reverse pattern is seen in the contemporary PC values. Here, the

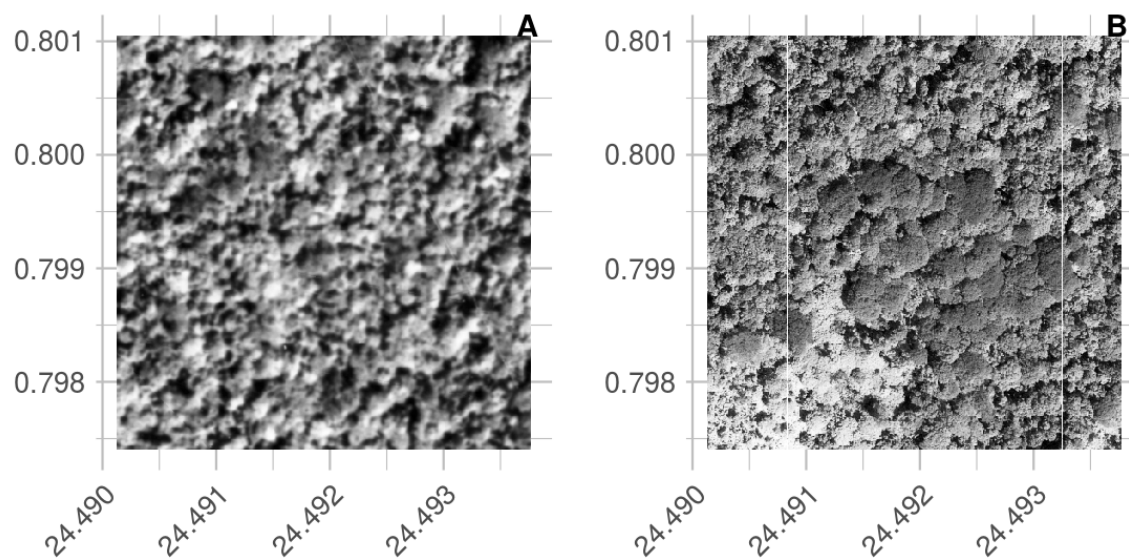


**Figure 6.** Visual comparison between a historical (A) and contemporary (B) permanent sampling plot. The site is currently listed as a mono-dominant *Brachystegia laurentii* stand. Note the structural differences with a 'coarse' canopy structure in the historical image compared to the more closed contemporary stand.

value of 0.54 exceeds those of most mono-dominant stands ( $0.35 \pm 0.08$ ), and is even further removed from the values noted for mixed forests ( $0.12 \pm 0.03$ ).

Using only small subsets around existing permanent sampling plots we show distinct differences between forest types, with PC values in both historical and contemporary imagery markedly higher for the mono-dominant forest types compared to all others (Appendix Figure 3). Provided that the young-regrowth and fallow permanent sampling plots have seen recent disturbance the Wilcoxon signed rank test on the mixed and mono-dominant plots between the historical and contemporary PC values did not show a significant difference ( $p > 0.05$ ). Similarly, no significant difference using PC values extracted from the whole scene analysis was noted ( $p > 0.05$ ). Any relationships between contemporary Geo-Eye data and permanent sampling plot measurements of Above Ground Biomass, stem density and species richness were non-significant ( $p > 0.05$ , Appendix Figures 4-6).

Furthermore, visual inspection of the scene wide analysis suggests historical scenes do not show landscape wide canopy features (Figure 7 A-B), unlike the contemporary scene (Figure 7 C-D). Where the FOTO algorithm picks up landscape features such as changes in texture across the contemporary Geo-Eye scene (e.g. the river valley as a diagonal line in Figure 7D), however, no corresponding landscape patterns are found by the FOTO algorithm in the historical orthomosaic.

#### 4. Discussion

Finely grained spatial data sources, such as remote sensing imagery, are rare before the satellite era (<1970). This lack of data limits our understanding of how forest structure has varied over longer time

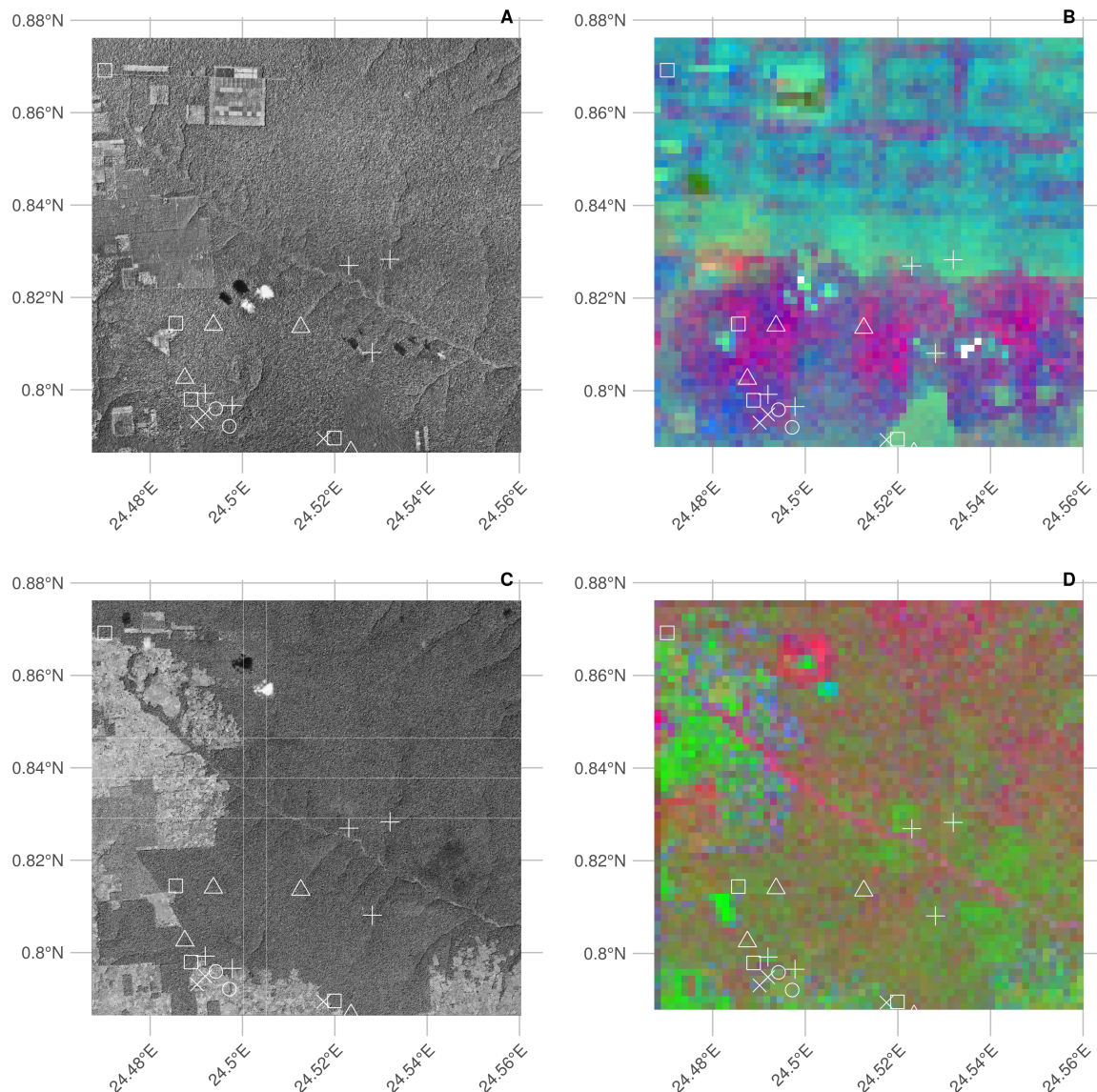


**Figure 7.** RGB visualizations of the first three principal components of scene wide FOTO texture analysis of historical and current (Geo-Eye) imagery. Current permanent sampling plots of mono-dominant, mixed, fallow and young (edge) forest plots are marked with open triangles, open circles, open squares and crosses, respectively.

301 periods in especially remote areas. Long term assessment can be extended by using large inventories  
302 of historical aerial survey data [27,28,54]. However, across the Congo Basin this data is rare, or difficult  
303 to access. Despite the difficulties in assessing hidden disturbances caused by deforestation, poorly  
304 recorded official assessments or simply those invisible to standard remote sensing techniques [6],  
305 remote sensing generally remains the best way to map and quantify LULCC [11]. Despite these  
306 challenges in recovery and validation we present a first analysis of LULCC using historical aerial  
307 survey data for the central Congo Basin. We used a combination of Structure-from-Motion and a  
308 convolutional neural net deep learning approach to map deforestation across a large extent, providing  
309 a long term view of LULCC in the central Congo Basin

310 *4.1. Data recovery challenges*

311 In our study the archive data recovered was limited to contact prints and therefore did not  
312 represent the true resolution of the original negative. In addition, analogue photography clearly  
313 produces a distinct softness compared to digital imagery (Figure 4). Despite favourable nadir image  
314 acquisitions [55] image softness combined with illumination effects between flight paths, and the  
315 self-similar nature of vast canopy expanses [56–58], limited our ability to provide wall-to-wall  
316 coverage of the entire dataset containing 334 images. Few man made features in the scenes also  
317 made georeferencing challenging. Although the village of Yangambi provided a range of buildings  
318 as (hard-edge) references, other areas within the central Congo Basin might have fewer permanent  
319 structures and would require the use of soft-edged landscape features (e.g. trees, river outflows).  
320 Research has shown that soft-edged features can help georeference scenes even when containing  
321 few man-made features [59], however accuracy becomes compromised. Our two step georeferencing  
322 approach resulted in a referencing accuracy of  $\sim 4.7 \pm 4.3$  m across reference points. However, it should  
323 be noted that referencing accuracy of the final scene is less constrained toward the edges of the scene.

324 *4.2. Land-use, Land-Cover change & Above Ground Carbon*

325 When classifying our orthomosaic into forest and non-forest states we favoured a deep learning  
326 supervised classification using a Convolutional Neural Network over manual segmentation to  
327 guarantee an “apples-to-apples” comparison between the historical and the contemporary GFC forest  
328 cover maps. We acknowledge that both classifications use different features, i.e. spectral or spatial data,  
329 but attain a similarly high accuracy of 97% and 99% [10], for the GFC and our CNN map respectively.  
330 Despite a number of challenges we were able to map and quantify a vast continuous area of tropical  
331 forest, with limited manual annotation requirements.

332 Our analysis shows that the majority of deforestation around Yangambi happened toward the late  
333 1950’s ( $162 \text{ km}^2$ ). Considerable regrowth has occurred since the aerial survey was executed ( $99 \text{ km}^2$ ),

and socio-economic instability prevented further large scale forest exploitation. In particular, many plantations have reached maturity and forest has re-established in previously cleared or disturbed areas. The majority of this forest recovery takes the form of isolated patches of forest but is offset by further deforestation of previously untouched forest. Generally, the function and structure of forests can be influenced by forest edges that are located up to 1km away however most effects are pronounced within the first 300m from the edge [60]. Our analysis of edge effects on AGC has shown that the influence is negligible 200m away from the edge. Phillips *et al.* [61] have shown similar weak responses to edge effects in the Amazon forest. Due to a lack of data on the extent (depth) of edge effects and their influence on AGC beyond 200m we did not include any estimates of carbon loss or gain within these zones. However, it must be stated that the influence of edges throughout the landscape was not marginal. as these areas would account for 132 km<sup>2</sup>. Thus edges could have a substantial negative [9] or positive [62] influence on AGC. Similarly, uncertainties in how to explicitly correct for plantations in the landscape present a further challenge. Thus although our estimates are only indicative they do underscore the important influence of landscape structure when carbon accounting. However, our findings do not indicate that deforestation in Congo basin is declining, on the contrary.

Over the past half century there has been a clear shift in land use in Yangambi (Figure 5). Land use has shifted away from for example a regular fishbone deforestation pattern that emerges when (large scale) agricultural interests dominate the landscape [63], to a more fragmented landscape (Figure 5D). The latter former? is consistent with historical land management at the time of the aerial survey [50]. These regular patterns have since been reversed because of a decrease in large scale intensive agriculture, replaced by ad-hoc small scale subsistence farming with large perimeter to area relationships (i.e. ragged edges). Consequently, edge effects in the current landscape are far more pronounced than in the historical scene.

Visual inspection of the images also suggests that reforestation within the historically cleared areas and experimental plots is not necessarily limited to areas far removed from more densely populated areas. For example, large reforested areas exist close to the Congo stream and Yangambi village itself (Fig. 5). Here, regional political components, such as land leases and large scale ownership could have played a role in safeguarding some of these areas for rewilling or sustainable management [64,65]. Despite widespread anthropogenic influences throughout the tropics [37] the retention of these forested areas show the potential of explicit or implicit protective policy measures (e.g. INERA concessions, Bustillo *et al.* [50]) on a multi-decadal time scale. Forest regrowth in non-continuous areas within Yangambi could increase landscape connectivity and help increase biodiversity [15].

367 Our analysis therefore provides an opportunity to highlight and study those regions that have  
368 previously suffered confirmed long-term disturbances, and those that have been restored since.  
369 Assessments of old plantations and recovering clear-cut forests can serve as a guide to help estimate  
370 carbon storage capacity and forest recovery rates in managed and unmanaged conditions [23,25,66]  
371 over the mid- to long-term, in support of rewilding and general forest restoration [15,64,65]. In addition,  
372 mapping long-term edge effects can further support research into issues such as receding forest edges  
373 [60].

374 *4.3. Canopy structure & FOTO texture analysis*

375 Finally the FOTO technique used to quantify relationships between canopy structure and forest  
376 characteristics rendered no valuable insights of either the historical orthomosaic or recent Geo-Eye  
377 scene. Similarly weak correlations were found previously by Solórzano *et al.* [53]. In contrast site  
378 based texture metric statistics did show correspondence between historical and contemporary satellite  
379 imagery. However, none of them were either consistent or significant. Although visual interpretation  
380 shows distinctly different canopy structures (Figure 5) the differences in how resolution is defined  
381 and issues related to image quality prevented us from quantifying these further. Unlike large scale  
382 studies by Ploton *et al.* [33] we could not scale this technique to historical data. We advise that future  
383 valorisation efforts should preferentially work from foto negatives (if available) to ensure optimal data  
384 quality in resolution, contrast and overall sharpness.

385 **5. Conclusion**

386 Given the impact of tropical forest disturbances on atmospheric CO<sub>2</sub> emissions, biodiversity and  
387 ecosystem productivity accurate long term reporting on land-cover and land-use change especially  
388 in the pre-satellite era is an imperative. Our analysis of historical aerial survey images of the Central  
389 Congo Basin provides a window into the state of the forest at the start of the anthropocene. Efforts to  
390 quantify canopy texture and their link to carbon storage had limited to no success. We have shown that  
391 historical aerial survey data can be used to quantify land-use and land-cover change using a highly  
392 automated workflow to quantify the structure and extent of forest cover change that can help assess  
393 the impact of fragmentation on above ground carbon stocks. We also show a shift from previously  
394 highly structured industrial deforestation of large areas, to discrete smallholder clearing for farming,  
395 increasing landscape fragmentation but also opportunity for substantial regrowth. Efforts to quantify  
396 canopy texture and their link to carbon storage had limited to no success. As such, our analysis  
397 provides insights into the state of rarely studied tropical forests and the rate at which deforestation  
398 and reforestation has taken place over a multi-decadal scale in the central Congo basin providing a

399 useful historical context to land-cover and land-use change spatial patterns for interpreting past and  
400 ongoing field research in the area.

## 401 6. Additional Information and Declarations

### 402 6.1. Data availability

403 Hufkens et al. (2019). A curated dataset of aerial survey images over the central Congo Basin,  
404 1958. Zenodo: doi.org/10.5281/zenodo.3547767. All data not included in the latter repository can be  
405 found bundled with the analysis code as listed below. Proprietary datasets (i.e. Geo-Eye data) are not  
406 shared, but purchase order numbers allow for acquisition of these datasets to ensure reproducibility.  
407 The Hansen *et al.* [10] image data is freely available from [the GFC project website](#).

### 408 6.2. Code availability

409 All analysis code is available as an R / python [67] projects (<https://khufkens.github.io/orthodrc>  
410 & [https://khufkens.github.io/orthodrc\\_cnn/](https://khufkens.github.io/orthodrc_cnn/)). The analysis relied heavily on the ‘raster’ [68],  
411 ‘RStoolbox’ [69], and ‘landscapemetrics’ [49] packages, while post-processing and plotting was  
412 facilitated by the ‘tidyverse’ ecosystem [70], ‘ggthemes’ [71], ‘scales’ [72] and ‘cowplot’ [73]. Additional  
413 plotting elements were formatted or provided by ‘sf’ [74] and ‘rnaturalearth’ [75] packages, respectively.  
414 I’m grateful for the contributions to the scientific community by the developers of these packages.

415 **Acknowledgments:** This research was supported through the Belgian Science Policy office COBECORE  
416 project (BELSPO; grant BR/175/A3/COBECORE). KH acknowledges funding from the European Union Marie  
417 Skłodowska-Curie Action (project number 797668). I’m grateful for the support of Thales D’Haulleville  
418 volunteering his time in scanning the images.

419 **Author Contributions:** K.H. conceived and designed the study, analyzed the data, prepared figures and tables,  
420 authored, reviewed and approved the final draft of the manuscript. T.d.H. scanned all image data. E.K. and T.d.H.  
421 provided plot based AGC estimates. T.D., K.J., E.K, H.B., P.S., F.V,S.M., M.A., J.V.D.B., H.V and L.W. reviewed the  
422 final manuscript.

423 **Conflicts of Interest:** The authors declare no conflict of interest. The founding sponsors had no role in the design  
424 of the study; in the collection, analyses, or interpretation of data; in the writing of the manuscript, an in the  
425 decision to publish the results.

## 426 References

- 427 1. Butsic, V.; Baumann, M.; Shortland, A.; Walker, S.; Kuemmerle, T. Conservation and conflict in the  
428 Democratic Republic of Congo: The impacts of warfare, mining, and protected areas on deforestation.  
429 *Biological Conservation* **2015**, *191*, 266–273. doi:10.1016/j.biocon.2015.06.037.
- 430 2. Laurance, W.F.; Delamônica, P.; Laurance, S.G.; Vasconcelos, H.L.; Lovejoy, T.E. Rainforest fragmentation  
431 kills big trees. *Nature* **2000**, *404*, 836–836. doi:10.1038/35009032.
- 432 3. Magnago, L.F.S.; Magrach, A.; Laurance, W.F.; Martins, S.V.; Meira-Neto, J.A.A.; Simonelli, M.; Edwards,  
433 D.P. Would protecting tropical forest fragments provide carbon and biodiversity cobenefits under REDD+?  
434 *Global Change Biology* **2015**, *21*, 3455–3468. doi:10.1111/gcb.12937.

- 435 4. Poorter, L.; Bongers, F. Leaf traits are good predictors of plant performance across 53 rain forest species.  
436 *Ecology* **2006**, *87*, 1733–1743. doi:10.1890/0012-9658(2006)87[1733:LTAGPO]2.0.CO;2.
- 437 5. Didham, R.K. Edge Structure Determines the Magnitude of Changes in Microclimate and Vegetation  
438 Structure in Tropical Forest Fragments. *Biotropica* **1999**, *31*, 17–30.
- 439 6. Peres, C.A.; Barlow, J.; Laurance, W.F. Detecting anthropogenic disturbance in tropical forests. *Trends in*  
440 *Ecology & Evolution* **2006**, *21*, 227–229. doi:10.1016/j.tree.2006.03.007.
- 441 7. Stark, S.C.; Leitold, V.; Wu, J.L.; Hunter, M.O.; de Castilho, C.V.; Costa, F.R.C.; McMahon, S.M.; Parker,  
442 G.G.; Shimabukuro, M.T.; Lefsky, M.A.; Keller, M.; Alves, L.F.; Schietti, J.; Shimabukuro, Y.E.; Brandão,  
443 D.O.; Woodcock, T.K.; Higuchi, N.; de Camargo, P.B.; de Oliveira, R.C.; Saleska, S.R. Amazon forest  
444 carbon dynamics predicted by profiles of canopy leaf area and light environment. *Ecology Letters* **2012**,  
445 *15*, 1406–1414. doi:10.1111/j.1461-0248.2012.01864.x.
- 446 8. Fauset, S.; Gloor, M.U.; Aidar, M.P.M.; Freitas, H.C.; Fyllas, N.M.; Marabesi, M.A.; Rochelle, A.L.C.;  
447 Shenkin, A.; Vieira, S.A.; Joly, C.A. Tropical forest light regimes in a human-modified landscape. *Ecosphere*  
448 **2017**, *8*, e02002. doi:10.1002/ecs2.2002.
- 449 9. Brinck, K.; Fischer, R.; Groeneveld, J.; Lehmann, S.; Dantas De Paula, M.; Pütz, S.; Sexton, J.O.; Song, D.;  
450 Huth, A. High resolution analysis of tropical forest fragmentation and its impact on the global carbon  
451 cycle. *Nature Communications* **2017**, *8*. doi:10.1038/ncomms14855.
- 452 10. Hansen, M.C.; Potapov, P.V.; Moore, R.; Hancher, M.; Turubanova, S.A.; Tyukavina, A.; Thau, D.; Stehman,  
453 S.V.; Goetz, S.J.; Loveland, T.R.; Kommareddy, A.; Egorov, A.; Chini, L.; Justice, C.O.; Townshend,  
454 J.R.G. High-Resolution Global Maps of 21st-Century Forest Cover Change. *Science* **2013**, *342*, 850–853.  
455 doi:10.1126/science.1244693.
- 456 11. Houghton, R.A.; House, J.I.; Pontratz, J.; van der Werf, G.R.; DeFries, R.S.; Hansen, M.C.; Le Quéré, C.;  
457 Ramankutty, N. Carbon emissions from land use and land-cover change. *Biogeosciences* **2012**, *9*, 5125–5142.  
458 doi:10.5194/bg-9-5125-2012.
- 459 12. Tyukavina, A.; Baccini, A.; Hansen, M.C.; Potapov, P.V.; Stehman, S.V.; Houghton, R.A.; Krylov, A.M.;  
460 Turubanova, S.; Goetz, S.J. Aboveground carbon loss in natural and managed tropical forests from 2000 to  
461 2012. *Environmental Research Letters* **2015**, *10*, 074002. doi:10.1088/1748-9326/10/7/074002.
- 462 13. van der Werf, G.R.; Morton, D.C.; DeFries, R.S.; Olivier, J.G.J.; Kasibhatla, P.S.; Jackson, R.B.; Collatz, G.J.;  
463 Randerson, J.T. CO<sub>2</sub> emissions from forest loss. *Nature Geoscience* **2009**, *2*, 737–738. doi:10.1038/ngeo671.
- 464 14. Barlow, J.; Lennox, G.D.; Ferreira, J.; Berenguer, E.; Lees, A.C.; Nally, R.M.; Thomson, J.R.; Ferraz, S.F.d.B.;  
465 Louzada, J.; Oliveira, V.H.F.; Parry, L.; Ribeiro de Castro Solar, R.; Vieira, I.C.G.; Aragão, L.E.O.C.; Begotti,  
466 R.A.; Braga, R.F.; Cardoso, T.M.; Jr, R.C.d.O.; Souza Jr, C.M.; Moura, N.G.; Nunes, S.S.; Siqueira, J.V.;  
467 Pardini, R.; Silveira, J.M.; Vaz-de Mello, F.Z.; Veiga, R.C.S.; Venturieri, A.; Gardner, T.A. Anthropogenic  
468 disturbance in tropical forests can double biodiversity loss from deforestation. *Nature* **2016**, *535*, 144–147.  
469 doi:10.1038/nature18326.
- 470 15. Van de Perre, F.; Willig, M.R.; Presley, S.J.; Bapeamoni Andemwana, F.; Beeckman, H.; Boeckx, P.; Cooleman,  
471 S.; de Haan, M.; De Kesel, A.; Dessein, S.; Grootaert, P.; Huygens, D.; Janssens, S.B.; Kearsley, E.; Kabeya,  
472 P.M.; Leponce, M.; Van den Broeck, D.; Verbeeck, H.; Würsten, B.; Leirs, H.; Verheyen, E. Reconciling  
473 biodiversity and carbon stock conservation in an Afrotropical forest landscape. *Science Advances* **2018**,  
474 *4*, eaar6603. doi:10.1126/sciadv.aar6603.
- 475 16. Lewis, S.L.; Lopez-Gonzalez, G.; Sonké, B.; Affum-Baffoe, K.; Baker, T.R.; Ojo, L.O.; Phillips, O.L.; Reitsma,  
476 J.M.; White, L.; Comiskey, J.A.; Djuikouo K, M.N.; Ewango, C.E.N.; Feldpausch, T.R.; Hamilton, A.C.;  
477 Gloor, M.; Hart, T.; Hladik, A.; Lloyd, J.; Lovett, J.C.; Makana, J.R.; Malhi, Y.; Mbago, F.M.; Ndangalasi,  
478 H.J.; Peacock, J.; Peh, K.S.H.; Sheil, D.; Sunderland, T.; Swaine, M.D.; Taplin, J.; Taylor, D.; Thomas, S.C.;  
479 Votere, R.; Wöll, H. Increasing carbon storage in intact African tropical forests. *Nature* **2009**, *457*, 1003–1006.  
480 Publisher: Earth and Biosphere Institute, School of Geography, University of Leeds, Leeds LS2 9JT, UK.  
481 s.l.lewis@leeds.ac.uk.
- 482 17. Verbeeck, H.; Boeckx, P.; Steppe, K. Tropical forests: include Congo basin. *Nature* **2011**, *479*, 179–179.
- 483 18. Lewis, S.L.; Sonke, B.; Sunderland, T.; Begne, S.K.; Lopez-Gonzalez, G.; van der Heijden, G.M.F.; Phillips,  
484 O.L.; Affum-Baffoe, K.; Baker, T.R.; Banin, L.; Bastin, J.F.; Beeckman, H.; Boeckx, P.; Bogaert, J.; De Canniere,  
485 C.; Chezeaux, E.; Clark, C.J.; Collins, M.; Djagbletey, G.; Djuikouo, M.N.K.; Droissart, V.; Doucet, J.L.;  
486 Ewango, C.E.N.; Fauset, S.; Feldpausch, T.R.; Foli, E.G.; Gillet, J.F.; Hamilton, A.C.; Harris, D.J.; Hart, T.B.;  
487 de Haulleville, T.; Hladik, A.; Hufkens, K.; Huygens, D.; Jeanmart, P.; Jeffery, K.J.; Kearsley, E.; Leal, M.E.;

- 488 Lloyd, J.; Lovett, J.C.; Makana, J.R.; Malhi, Y.; Marshall, A.R.; Ojo, L.; Peh, K.S.H.; Pickavance, G.; Poulsen,  
489 J.R.; Reitsma, J.M.; Sheil, D.; Simo, M.; Steppe, K.; Taedoumg, H.E.; Talbot, J.; Taplin, J.R.D.; Taylor, D.;  
490 Thomas, S.C.; Toirambe, B.; Verbeeck, H.; Vleminckx, J.; White, L.J.T.; Willcock, S.; Woell, H.; Zemagho, L.  
491 Above-ground biomass and structure of 260 African tropical forests. *Philosophical Transactions of the Royal  
492 Society B: Biological Sciences* **2013**, *368*, 20120295–20120295. doi:10.1098/rstb.2012.0295.
- 493 19. Kearsley, E.; de Haulleville, T.; Hufkens, K.; Kidimbu, A.; Toirambe, B.; Baert, G.; Huygens, D.; Kebede,  
494 Y.; Defourny, P.; Bogaert, J.; Beeckman, H.; Steppe, K.; Boeckx, P.; Verbeeck, H. Conventional tree  
495 height-diameter relationships significantly overestimate aboveground carbon stocks in the Central Congo  
496 Basin. *Nature communications* **2013**, *4*, 2269. doi:10.1038/ncomms3269.
- 497 20. Doetterl, S.; Kearsley, E.; Bauters, M.; Hufkens, K.; Lisingo, J.; Baert, G.; Verbeeck, H.; Boeckx, P.  
498 Aboveground vs. Belowground Carbon Stocks in African Tropical Lowland Rainforest: Drivers and  
499 Implications. *Plos One* **2015**, *10*, e0143209. doi:10.1371/journal.pone.0143209.
- 500 21. Ramankutty, N.; Foley, J.A. Estimating historical changes in global land cover: Croplands from 1700 to  
501 1992. *Global Biogeochemical Cycles* **1999**, *13*, 997–1027. doi:10.1029/1999GB900046.
- 502 22. DeFries, R.S.; Houghton, R.A.; Hansen, M.C.; Field, C.B.; Skole, D.; Townshend, J. Carbon emissions from  
503 tropical deforestation and regrowth based on satellite observations for the 1980s and 1990s. *Proceedings of  
504 the National Academy of Sciences* **2002**, *99*, 14256–14261. doi:10.1073/pnas.182560099.
- 505 23. Sader, S.A.; Joyce, A.T. Deforestation Rates and Trends in Costa Rica, 1940 to 1983. *Biotropica* **1988**, *20*, 11.  
506 doi:10.2307/2388421.
- 507 24. Houghton, R. How well do we know the flux of CO<sub>2</sub> from land-use change? *Tellus B: Chemical and Physical  
508 Meteorology* **2010**, *62*, 337–351. doi:10.1111/j.1600-0889.2010.00473.x.
- 509 25. Achard, F.; Beuchle, R.; Mayaux, P.; Stibig, H.J.; Bodart, C.; Brink, A.; Carboni, S.; Desclée, B.; Donnay, F.;  
510 Eva, H.D.; Lupi, A.; Raši, R.; Seliger, R.; Simonetti, D. Determination of tropical deforestation rates and  
511 related carbon losses from 1990 to 2010. *Global Change Biology* **2014**, *20*, 2540–2554. doi:10.1111/gcb.12605.
- 512 26. Mitchard, E.T.A. The tropical forest carbon cycle and climate change. *Nature* **2018**, *559*, 527–534.  
513 doi:10.1038/s41586-018-0300-2.
- 514 27. Song, D.X.; Huang, C.; Sexton, J.O.; Channan, S.; Feng, M.; Townshend, J.R. Use of Landsat and  
515 Corona data for mapping forest cover change from the mid-1960s to 2000s: Case studies from the Eastern  
516 United States and Central Brazil. *ISPRS Journal of Photogrammetry and Remote Sensing* **2015**, *103*, 81–92.  
517 doi:10.1016/j.isprsjprs.2014.09.005.
- 518 28. Nita, M.D.; Munteanu, C.; Gutman, G.; Abrudan, I.V.; Radloff, V.C. Widespread forest cutting in the  
519 aftermath of World War II captured by broad-scale historical Corona spy satellite photography. *Remote  
520 Sensing of Environment* **2018**, *204*, 322–332. doi:10.1016/j.rse.2017.10.021.
- 521 29. Giordano, S.; Le Bris, A.; Mallet, C. Toward automatic georeferencing of archival aerial photogrammetric  
522 surveys. *ISPRS Annals of Photogrammetry, Remote Sensing and Spatial Information Sciences* **2018**, IV-2, 105–112.  
523 doi:10.5194/isprs-annals-IV-2-105-2018.
- 524 30. Buitenwerf, R.; Bond, W.J.; Stevens, N.; Trollope, W.S.W. Increased tree densities in South African  
525 savannas: >50 years of data suggests CO<sub>2</sub> as a driver. *Global Change Biology* **2012**, *18*, 675–684.  
526 doi:10.1111/j.1365-2486.2011.02561.x.
- 527 31. Okeke, F.; Karnieli, A. Methods for fuzzy classification and accuracy assessment of historical aerial  
528 photographs for vegetation change analyses. Part I: Algorithm development. *International Journal of Remote  
529 Sensing* **2006**, *27*, 153–176. doi:10.1080/01431160500166540.
- 530 32. Frankl, A.; Seghers, V.; Stal, C.; De Maeyer, P.; Petrie, G.; Nyssen, J. Using image-based modelling  
531 (SfM-MVS) to produce a 1935 ortho-mosaic of the Ethiopian highlands. *International Journal of Digital Earth*  
532 **2015**, *8*, 421–430. doi:10.1080/17538947.2014.942715.
- 533 33. Ploton, P.; Pélassier, R.; Proisy, C.; Flavenot, T.; Barbier, N.; Rai, S.N.; Couteron, P. Assessing aboveground  
534 tropical forest biomass using Google Earth canopy images. *Ecological Applications* **2012**, *22*, 993–1003.
- 535 34. Couteron, P.; Pelissier, R.; Nicolini, E.a.; Paget, D. Predicting tropical forest stand structure parameters  
536 from Fourier transform of very high-resolution remotely sensed canopy images. *Journal of Applied Ecology*  
537 **2005**, *42*, 1121–1128. doi:10.1111/j.1365-2664.2005.01097.x.
- 538 35. Barbier, N.; Couteron, P.; Proisy, C.; Malhi, Y.; Gastellu-Etchegorry, J.P. The variation of apparent crown  
539 size and canopy heterogeneity across lowland Amazonian forests. *Global Ecology and Biogeography* **2010**,  
540 *19*, 72–84. doi:10.1111/j.1466-8238.2009.00493.x.

- 541 36. Willcock, S.; Phillips, O.L.; Platts, P.J.; Swetnam, R.D.; Balmford, A.; Burgess, N.D.; Ahrends, A.; Bayliss,  
542 J.; Doggart, N.; Doody, K.; Fanning, E.; Green, J.M.H.; Hall, J.; Howell, K.L.; Lovett, J.C.; Marchant, R.;  
543 Marshall, A.R.; Mbilinyi, B.; Munishi, P.K.T.; Owen, N.; Topp-Jorgensen, E.J.; Lewis, S.L. Land cover  
544 change and carbon emissions over 100 years in an African biodiversity hotspot. *Global Change Biology* **2016**,  
545 22, 2787–2800. doi:10.1111/gcb.13218.
- 546 37. Lewis, S.L.; Maslin, M.A. Defining the Anthropocene. *Nature* **2015**, 519, 171–180. doi:10.1038/nature14258.
- 547 38. Bauters, M.; Ampoorter, E.; Huygens, D.; Kearsley, E.; De Haulleville, T.; Sellan, G.; Verbeeck, H.; Boeckx,  
548 P.; Verheyen, K. Functional identity explains carbon sequestration in a 77-year-old experimental tropical  
549 plantation. *Ecosphere* **2015**, 6, art198. doi:10.1890/ES15-00342.1.
- 550 39. Zuiderveld, K. Contrast Limited Adaptive Histogram Equalization. In *Graphics GEMs IV*; Academic Press:  
551 San Diego, CA, USA, 1994; pp. 474–485.
- 552 40. Ullman, S. The Interpretation of Structure from Motion. *Proceedings of the Royal Society of London. Series B,  
553 Biological Sciences* **1979**, 203, 405–426.
- 554 41. QGIS Development team,. QGIS Geographic Information System., 2018.
- 555 42. Ronneberger, O.; Fischer, P.; Brox, T. U-Net: Convolutional Networks for Biomedical Image Segmentation.  
556 In *Medical Image Computing and Computer-Assisted Intervention – MICCAI 2015*; Navab, N.; Hornegger, J.;  
557 Wells, W.M.; Frangi, A.F., Eds.; Springer International Publishing: Cham, 2015; Vol. 9351, pp. 234–241.  
558 doi:10.1007/978-3-319-24574-4\_28.
- 559 43. Chollet, F. *Keras*; GitHub, 2015.
- 560 44. Yakubovskiy, P. *Segmentation Models*; GitHub, 2019.
- 561 45. Martín Abadi.; Ashish Agarwal.; Paul Barham.; Eugene Brevdo.; Zhifeng Chen.; Craig Citro.; Greg S.  
562 Corrado.; Andy Davis.; Jeffrey Dean.; Matthieu Devin.; Sanjay Ghemawat.; Ian Goodfellow.; Andrew  
563 Harp.; Geoffrey Irving.; Michael Isard.; Jia, Y.; Rafal Jozefowicz.; Lukasz Kaiser.; Manjunath Kudlur.; Josh  
564 Levenberg.; Dandelion Mané.; Rajat Monga.; Sherry Moore.; Derek Murray.; Chris Olah.; Mike Schuster.;  
565 Jonathon Shlens.; Benoit Steiner.; Ilya Sutskever.; Kunal Talwar.; Paul Tucker.; Vincent Vanhoucke.; Vijay  
566 Vasudevan.; Fernanda Viégas.; Oriol Vinyals.; Pete Warden.; Martin Wattenberg.; Martin Wicke.; Yuan Yu.;  
567 Xiaoqiang Zheng. *TensorFlow: Large-Scale Machine Learning on Heterogeneous Systems*; 2015.
- 568 46. Buscombe, D.; Ritchie, A. Landscape Classification with Deep Neural Networks. *Geosciences* **2018**, 8, 244.  
569 doi:10.3390/geosciences8070244.
- 570 47. Kingma, D.P.; Ba, J. Adam: A Method for Stochastic Optimization. *arXiv:1412.6980 [cs]* **2017**. arXiv:  
571 1412.6980.
- 572 48. Dale, M.R.T. *Spatial pattern analysis in plant ecology*; Cambridge studies in ecology, Cambridge University  
573 Press: Cambridge ; New York, 1999.
- 574 49. Hesselbarth, M.H.K.; Sciaiani, M.; With, K.A.; Wiegand, K.; Nowosad, J. landscapemetrics: an open-source  
575 R tool to calculate landscape metrics. *Ecography* **2019**.
- 576 50. Bustillo, E.; Raets, L.; Beeckman, H.; Bourland, N.; Rousseau, M.; Hubau, W.; De Mil, T. Evaluation du  
577 potentiel énergétique de la biomasse aérienne ligneuse des anciennes plantations de l'INERA Yangambi.  
578 Technical report, CIFOR, 2018.
- 579 51. Couturon, P. Quantifying change in patterned semi-arid vegetation by Fourier analysis of digitized aerial  
580 photographs. *International Journal of Remote Sensing* **2002**, 23, 3407–3425. doi:10.1080/01431160110107699.
- 581 52. Hufkens, K. foto: an R implementation of the "fourier transform textural ordination (foto)" method., 2019.
- 582 53. Solórzano, J.V.; Gallardo-cruz, J.A.; González, E.J.; Peralta-carreta, C.; Hernández-gómez, M.; Oca,  
583 A.F.m.D.; Cervantes-jiménez, L.G.; Solórzano, J.V.; Gallardo-cruz, J.A.; González, E.J.; Peralta-carreta,  
584 C.; Hernández-gómez, M.; Oca, A.F.m.D.; Cervantes-jiménez, L.G. Contrasting the potential of  
585 Fourier transformed ordination and gray level co-occurrence matrix textures to model a tropical swamp  
586 forest 's structural and diversity attributes. *Journal of Applied Remote Sensing* **2018**, 12, 036006.  
587 doi:10.1117/1.JRS.12.036006.
- 588 54. Kadmon, R.; Harari-Kremer, R. Studying Long-Term Vegetation Dynamics Using Digital  
589 Processing of Historical Aerial Photographs. *Remote Sensing of Environment* **1999**, 68, 164–176.  
590 doi:10.1016/S0034-4257(98)00109-6.
- 591 55. Verhoeven, G. BRDF and its Impact on Aerial Archaeological Photography: BRDF and its impact on aerial  
592 archaeologal photography. *Archaeological Prospection* **2017**, 24, 133–140. doi:10.1002/arp.1559.

- 593 56. Park, J.Y.; Muller-Landau, H.C.; Lichstein, J.W.; Rifai, S.W.; Dandois, J.P.; Bohlman, S.A. Quantifying Leaf  
594 Phenology of Individual Trees and Species in a Tropical Forest Using Unmanned Aerial Vehicle (UAV)  
595 Images. *Remote Sensing* **2019**, *11*, 1534. doi:10.3390/rs11131534.
- 596 57. Simini, F.; Anfodillo, T.; Carrer, M.; Banavar, J.R.; Maritan, A. Self-similarity and scaling  
597 in forest communities. *Proceedings of the National Academy of Sciences* **2010**, *107*, 7658–7662.  
598 doi:10.1073/pnas.1000137107.
- 599 58. Sole, R.V.; Manrubia, S.C. Self-similarity in rain forests: evidence for a critical state. *Physical Review E* **1995**,  
600 51, 6250 – 6253.
- 601 59. Hughes, M.L.; McDowell, P.F.; Marcus, W.A. Accuracy assessment of georectified aerial photographs:  
602 Implications for measuring lateral channel movement in a GIS. *Geomorphology* **2006**, *74*, 1–16.  
603 doi:10.1016/j.geomorph.2005.07.001.
- 604 60. Gascon, C.; Williamson, G.B.; Fonseca, G.A.B.d. Receding Forest Edges and Vanishing Reserves. *Science,*  
605 *New Series* **2000**, *288*, 1356–1358.
- 606 61. Phillips, O.L.; Rose, S.; Mendoza, A.M.; Vargas, P.N. Resilience of Southwestern Amazon Forests to  
607 Anthropogenic Edge Effects. *Conservation Biology* **2006**, *20*, 1698–1710. doi:10.1111/j.1523-1739.2006.00523.x.
- 608 62. Reinmann, A.B.; Hutyra, L.R. Edge effects enhance carbon uptake and its vulnerability to climate  
609 change in temperate broadleaf forests. *Proceedings of the National Academy of Sciences* **2017**, *114*, 107–112.  
610 doi:10.1073/pnas.1612369114.
- 611 63. Arima, E.Y.; Walker, R.T.; Perz, S.; Souza, C. Explaining the fragmentation in the Brazilian Amazonian  
612 forest. *Journal of Land Use Science* **2015**, pp. 1–21. doi:10.1080/1747423X.2015.1027797.
- 613 64. Arima, E.Y.; Barreto, P.; Araújo, E.; Soares-Filho, B. Public policies can reduce tropical deforestation: Lessons  
614 and challenges from Brazil. *Land Use Policy* **2014**, *41*, 465–473. doi:10.1016/j.landusepol.2014.06.026.
- 615 65. Larson, A.M. Forest tenure reform in the age of climate change: Lessons for REDD+. *Global Environmental  
616 Change* **2011**, *21*, 540–549. doi:10.1016/j.gloenvcha.2010.11.008.
- 617 66. Gourlet-Fleury, S.; Mortier, F.; Fayolle, A.; Baya, F.; Ouédraogo, D.; Bénédet, F.; Picard, N. Tropical forest  
618 recovery from logging: a 24 year silvicultural experiment from Central Africa. *Philosophical Transactions of  
619 the Royal Society B: Biological Sciences* **2013**, *368*, 20120302. doi:10.1098/rstb.2012.0302.
- 620 67. R Core Team. *R: A Language and Environment for Statistical Computing*; R Foundation for Statistical  
621 Computing: Vienna, Austria, 2019.
- 622 68. Hijmans, R.J. *raster: Geographic Data Analysis and Modeling*; 2019.
- 623 69. Leutner, B.; Horning, N.; Schwalb-Willmann, J. *RStoolbox: Tools for Remote Sensing Data Analysis*; 2019.
- 624 70. Wickham, H. *tidyverse: Easily Install and Load the 'Tidyverse'*; 2017.
- 625 71. Arnold, J.B. *ggthemes: Extra Themes, Scales and Geoms for 'ggplot2'*; 2019.
- 626 72. Wickham, H. *scales: Scale Functions for Visualization*; 2018.
- 627 73. Wilke, C.O. *cowplot: Streamlined Plot Theme and Plot Annotations for 'ggplot2'*; 2019.
- 628 74. Pebesma, E. Simple Features for R: Standardized Support for Spatial Vector Data. *The R Journal* **2018**,  
629 *10*, 439–446. doi:10.32614/RJ-2018-009.
- 630 75. South, A. *rnatnuralearth: World Map Data from Natural Earth*; 2017.

631 © 2019 by the authors. Submitted to *Remote Sens.* for possible open access publication  
632 under the terms and conditions of the Creative Commons Attribution (CC BY) license  
633 (<http://creativecommons.org/licenses/by/4.0/>).